*Environ. Sci. Technol.* **1998**, *32,* 3068−3076

# Application of Elastic Lidar to $PM_{10}$ Emissions from Agricultural Nonpoint Sources

BRITT A. HOLMÉN,*,† WILLIAM E. EICHINGER,‡ AND ROBERT G. FLOCCHINI†

*Crocker Nuclear Laboratory, University of California, Davis, California 95616, and Iowa Institute for Hydraulics Research, University of Iowa, Iowa City, Iowa 52242*

$PM_{10}$ emissions from nonpoint sources need to be quantified in order to effectively meet air quality standards. In California's Central Valley, agricultural operations are highly complex but significant sources of $PM_{10}$ that are difficult to quantify using point sampling arrays. A remote sensing technique, light detection and ranging (lidar), using a small field portable, fast-scanning lidar shows great potential for measuring $PM_{10}$ emissions from agricultural nonpoint sources. The qualitative capabilities of the lidar instrument are demonstrated for land preparation operations at a wheat field. The range (>5 km), spatial resolution (2.5 m) and fast response times (s) of the lidar allow the following: (i) plume dynamics to be described in detail and eventually to be modeled as a function of source fluctuations and environmental conditions, (ii) measurements of average wind speed and direction over 50−100 m scales, (iii) quantitative determination of the fraction of dust missed by point sampling arrays, and (iv) currently provide unparalleled information on nonpoint source emission variability, both temporally and spatially. The lidar data indicate the line source nature of plumes from tractor operations and suggest that fast lidar 2D vertical scans downwind of nonpoint sources will provide the best $PM_{10}$ emission factor measurements. Widespread use of lidar for direct quantitative emission factor measurement depends on careful determination of particulate matter backscatter−mass calibration relationships.

## Introduction

Particulate matter of aerodynamic diameter less than or equal to 10 $\mu$m, $PM_{10}$, is a regulated National Ambient Air Quality pollutant. $PM_{10}$ is directly emitted from a wide range of industrial point sources (power plants, incinerator fly ash, cement plants), mobile sources (automobiles and trucks), and nonpoint sources such as agricultural operations (land tilling, harvesting, cattle ranches) and construction sites.

Little is known about the quantity, composition, fluxes, and transport distances of agricultural "fugitive" dust and its contribution to $PM_{10}$ exceedances. Agricultural dust sources are difficult to quantify, relative to stationary point sources, chiefly due to the complexity and nonpoint nature of agricultural operations. Agricultural sources vary both temporally and spatially (i.e., daily and seasonally varying activities, inhomogeneous wide area sources, nonstandard agricultural practices and implements), and $PM_{10}$ emissions depend on locally variable soil, hydrological, and meteorological conditions. Understanding how these individual factors affect PM emissions is critical to developing accurate air quality models for agricultural operations under varying environmental conditions.

In certain arid agricultural locations, such as the Central Valley of California, agricultural operations may be one of the most important sources of airborne particulate matter contributing to the "nonattainment" status of this air quality region. The problem is compounded by the semi-arid climate and the fine soil texture (silty clay) in the San Joaquin Valley. Furthermore, agricultural aerosols, especially plant organic debris, while occurring as particles of relatively large physical dimension, can be of such low density that they may remain airborne and travel significant distances from their source. Due to their small size and large surface area, the finer particulate matter may also transport adsorbed chemicals (i.e., pesticides, fertilizer) to downwind locations (urban areas, water bodies, sensitive crops) (*1*−*3*). Quantifying the PM contributions from agricultural sources is requisite to understanding the potential impact these particles have on human and environmental health as well as developing accurate regional air quality models.

Despite the need to quantify agricultural PM sources, only a few measurements have been reported to date using point samplers positioned either immediately downwind of the agricultural operation (*4*−*6*) or positioned on the tractor implement (*7*, *8*). Unfortunately, point measurements cannot reasonably capture the entire PM plume generated across an agricultural source. Three factors contribute to the limited ability of conventional point PM samplers to quantify PM emissions from these operations: (i) the large spatial dimensions of agricultural sources, the spatial irregularity of dust plumes, and the small number of point sampling locations generally used results in under-sampling of the dust plume; (ii) the spatial variability in the PM source location (i.e., tractor) within the entire field as the operation traverses the field means the direction and distance from a point sampler to the PM source changes with time; and (iii) the vertical extent of point sampling is limited to the height of portable towers. Furthermore, point samplers located on the tractor do not reliably quantify the amount of $PM_{10}$ that will be emitted from a field due to particle gravitational settling and turbulence-induced dry deposition within the field boundaries.

All of these point sampler limitations can be overcome using elastic lidar remote sensing, a technique that offers high temporal (seconds) and spatial resolution (2.5 m) and extensive analysis range (over 5 km) capabilities. The tradeoff with lidar is that samples of the dust are not available for chemical analysis, and the lidar signal (optical backscatter) depends strongly on particle composition (refractive index), shape, and size distribution (*9*). Therefore, field calibration of the lidar signal with real-world agricultural PM will be required in order to convert the backscatter signal directly into $PM_{10}$ emission factors (e.g., mass or particle number per unit measure of agricultural activity) (see Discussion).

Despite the present limitation for quantifying $PM_{10}$ emission factors directly with the lidar, the lidar technique can currently provide important *qualitative* data on agricultural $PM_{10}$ emissions and can be used to improve the point sampling methods presently used to estimate $PM_{10}$ emission factors from nonpoint agricultural sources. Pre-

* Corresponding author e-mail: holmen@crocker.ucdavis.edu; phone: (530)752-1213; fax: (530)752-4107.
† University of California.
‡ University of Iowa.


S0013-936X(98)00176-X CCC: $15.00 
Published on Web 09/04/1998

liminary results shown here from exploratory field experiments during wheat harvesting and first disk harrowing in the San Joaquin Valley demonstrate the UC Davis miniature elastic lidar instrument's capabilities and the contributions lidar can make to understanding PM generation and transport from nonpoint sources. Coupled with a few time-integrated point filter samples, the lidar technique should greatly improve understanding of PM emissions from agricultural operations and lead to future development of cost-effective emission control strategies.

## Methods

**The Miniature Elastic Lidar.** Lidar is an acronym for *li*ght *d*etection *a*nd *r*anging. Lidar systems operate on similar principles as radar (*ra*dio *d*etection and *r*anging), but use a pulsed laser to scan through the atmosphere over a desired range of directions and elevations. In elastic lidar, light scattered back toward the lidar instrument from molecules and particles in the atmosphere is collected by a telescope and measured with a photodetector. The signal is digitized and analyzed by a computer to create a real-time detailed image of relative aerosol concentrations within the scanned region.

Using a short (~10 ns) pulse of infrared laser light, the UC Davis miniature elastic lidar (Figure 1) is a small (~2 $m^3$ and 100 kg) scanning lidar that uses elastic backscattering to obtain information on the distribution and properties of atmospheric aerosols with a range resolution of 2.5 m. A Nd:YAG laser operating at 1.064 $\mu$m is used as the light source. The laser beam illuminates a volume of the atmosphere ~2 m long and of diameter that varies with range due to the laser divergence angle of 3 mrad (beam diameter ~0.5 cm at instrument). The laser is attached directly to the top of a 26 cm, f/10, Cassegrain telescope that acts as the lidar receiver. The telescope–laser system turns rapidly through 180 deg horizontally and 90 deg vertically using computer-controlled motors incorporated into the telescope mount (Figure 1).

Behind the telescope, the light passes through an interference filter and a lens system that focuses the light on a 3 mm diameter, IR-enhanced silicon avalanche photodiode. The signal is amplified as part of the detector system and fed to a 12-bit digitizer. Two detectors mounted in the periscope sample the outgoing laser pulse ($P_o$, Figure 1b) and produce signals that are used to correct for pulse-to-pulse variations in the laser energy and to also serve as a timing marker to start the digitization process. A series of pulses are summed to make a single "scan" along one line-of-sight (LOS). A number of scans along multiple lines-of-sight are used to build up a two-dimensional map of relative atmospheric aerosol concentrations. The computer runs preprogrammed scan routines that control the entire lidar system and also processes the raw lidar information to present a real-time color display of spatial aerosol concentrations. Specifications for the UCD miniature elastic lidar are given in Table 1, and Figure 1a shows the lidar deployed in the field. Unlike previous lidar instruments, this lidar is capable of fast scanning, is lightweight and field portable, has low electrical power requirements, and its simple design enables effortless field operation in almost any location.

The diverging 1.064 $\mu$m laser beam is not eye-safe at ranges less than approximately 1 km. Therefore, both spotters and a video camera mounted on top of the periscope allow the lidar operator to monitor the beam location at all times during scanning and to block the laser beam whenever objects (airplanes, people) approach the lidar line-of-sight.

**The Lidar Signal.** The return power received by the lidar from a given range $R$, $P(R)$:


**FIGURE 1. (a) UC Davis miniature elastic lidar deployed in the field during the wheat harvest. (b) Schematic of the main components of the lidar system. The scanning system, the telescope receiver with laser, and the periscope assembly are the only components visible in panel a. The computer and displays are located 25 ft away inside a truck.**

$$P(R) = P_o \frac{A_r}{R^2} \beta(R) \frac{c\tau_L}{2} \exp[-2\int_0^R \alpha(r)\, dr] \qquad (1)$$

is a function of the outgoing laser power [$P_o$, W], the volume backscatter coefficient [$\beta(R)$, $m^{-1}$ $sr^{-1}$], the volume extinction coefficient [$\alpha$(r), $m^{-1}$], and three constants ($A_r$, $c$, $\tau_L$) (*9*, *10*). $A_r$ is a system coefficient that takes into account the effective area of the telescope, the transmission efficiency of the optical train, and the detector quantum efficiency; $c$ is the velocity of light (m/s); and $\tau_L$ is the laser pulse duration (s). Combining the system constants into a single term, the lidar equation becomes

$$P(R) = P_o \kappa \frac{\beta(R)}{R^2} \exp[-2\int_0^R \alpha(r)\, dr] \qquad (2)$$

where $\kappa = A_r c\tau_L/2$ is the lidar hardware calibration constant.

The backscatter and extinction coefficients at each range, $\beta(R)$ and $\alpha(r)$, are not independently quantified by a single wavelength lidar system. Therefore, assumptions about the background atmospheric extinction properties are usually

**TABLE 1. UCD Miniature Elastic Lidar Specifications**

| | |
|---|---|
| laser | Q-switched Nd:YAG: 1.064 $\mu$m, 100 mJ, 3 mrad divergence, 12 ns pulse, 50 Hz (Big Sky Laser, CFR200) |
| telescope | 10 in. diameter, Cassegrain f/10, 5 mrad FOV[a] (Meade LX50) |
| detector | enhanced Si avalanche photodiode (Analog Modules 710-352A) |
| $P_{out}$ detectors | high-speed silicon photodetectors (Thorlabs, DET-100), 1.064 $\mu$m narrowband filter (Barr Associates, 3 nm) |
| computer | Pentium 133 MHz, 16 MB RAM, 2.1 GB hard drive; 1 GB JAZ drive; dual flat panel video displays |
| digitizer | 12-bit 60 MHz, dual channel (Signatec DA60) |
| scanning system | Azimuth rotary stage (180:1), stepper motors & encoders, elevation right angle reducer (100:1), AT6400 controller (Compumotor) |

[a] FOV, field of view.

made in order to extract backscatter information directly from the lidar signal (*11, 12*). Because Rayleigh scattering due to atmospheric gas molecules ($\sim 1/\lambda^4$) is insignificant relative to particle backscatter at 1 $\mu$m wavelengths (*13*), the lidar signal gives *particle* attenuation (extinction + backscatter) information directly. This is especially true for many polluted areas (*9*). The lidar signal is a function of both the quantity of particles detected as well as the backscattering efficiency of the individual particles. Since particle backscatter is a function of composition, size, and shape, variations in any of these parameters will affect the lidar signal.

Because the backscattered light intensity is a strong function of particle size relative to the wavelength of the incident light (*14*), particles with diameters close to the laser's wavelength will scatter more light back to the lidar than larger particles, which tend to forward scatter the light (*15*). Based on Mie theory (*14, 15*), the 1.064 $\mu$m wavelength of the UCD lidar means particles between 0.5 and 5 $\mu$m diameter are responsible for most of the detected signal; these particles are also collected in our $PM_{10}$ point samplers. Field comparisons of the elastic lidar data with particle size distributions have shown that the 1.064 $\mu$m lidar signal correlates strongly with particle number concentrations in the 0.5−5 $\mu$m range but does not track well with smaller and larger particle sizes (*16*).

Few studies have examined the in situ optical properties of soil-derived dust. Laboratory studies have, however, documented the infrared absorption character of soils in the 700−1300 $cm^{-1}$ (14.2−7.7 $\mu$m) region (*17*) and backscatter signatures at $CO_2$ laser wavelengths (10.6 $\mu$m) (*18*). Both of these studies highlight the importance of a few soil minerals as dust components: silica, clays, and calcium carbonate. For agricultural soils, organic detritus will contribute to the imaginary refractive index; however, this component will be minor as compared to the mineral fraction for the majority of soils. Thus, for a single agricultural field, the particle composition and size properties should not vary greatly relative to the differences in particle number concentration within a given dust cloud. Therefore, for soil-derived PM, variation in particle number density should be the dominant factor affecting the lidar return signal at a given field site. As discussed in more detail below, field calibration of the lidar to the optical properties ($\alpha, \beta$) of soil-derived $PM_{10}$ suspended by agricultural operations for different mass concentrations will lead to quantitative interpretation of the lidar signal.

One additional factor in using the UCD lidar system to monitor agricultural operations is the instrument's useful range. To prevent detector overload from near-field returns, the periscope system (Figure 1b) was designed so the distance where the outgoing laser beam coincides with the field-of-view of the telescope is at a range of 300 m. This means that the lidar must be located at least 300 m from the sampling area of interest. This does not pose a detection problem for agricultural fieldwork since the lidar has a maximum range of 6−10 km, depending on atmospheric conditions. With a range resolution of 2.5 m and temporal resolution of tens of seconds for moderately sized two-dimensional scans, the lidar is capable of producing very detailed maps of relative PM distribution across an agricultural operation.

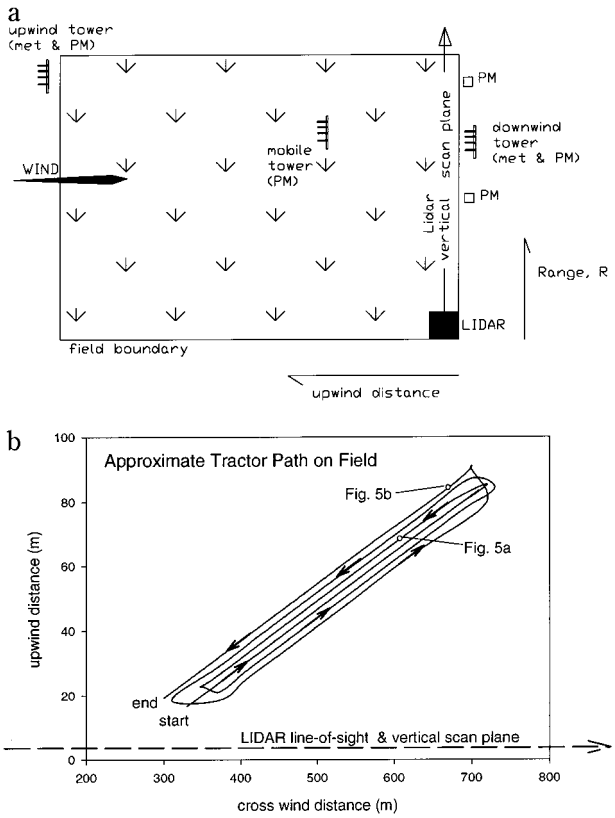


**FIGURE 2. (a) PM point sampler, meteorological towers, and lidar sampling layout during field sampling. The lidar scan plane is near the downwind edge of the field and pointed in the crosswind direction in order to capture the entire plume leaving the field. (b) Map view of approximate tractor path on the field during the disk harrowing operations. The diagram is oriented with the downwind edge of the field at the bottom in this figure. Note that the tractor was disking at an angle to the field boundaries in order to smooth out the rows of harvested wheat stubble that were planted parallel to the downwind field edge. This diagram is schematic and shows how the disk path is donut-like in order to allow the tractor to make wide turns yet still cover the entire field with the disk. The relative positions of the tractor during collection of the scans in Figure 5 are noted on the tractor path lines.**

**Field Sampling Layout.** One week of field work with the lidar was conducted during wheat harvesting, first disk harrowing, and ripping at two fields in the San Joaquin Valley, CA. A full array of stationary PM point samplers was deployed during the initial lidar tests. The full array includes upwind and downwind towers with PM samplers at multiple heights (1, 3, and 9 m) and two crosswind 3-m PM samplers (Figure 2a). In addition, a mobile 9-m tower, fastened to a pickup bed, was used mid-field. The lidar was positioned at the edge of the field and pointed crosswind so that the lidar

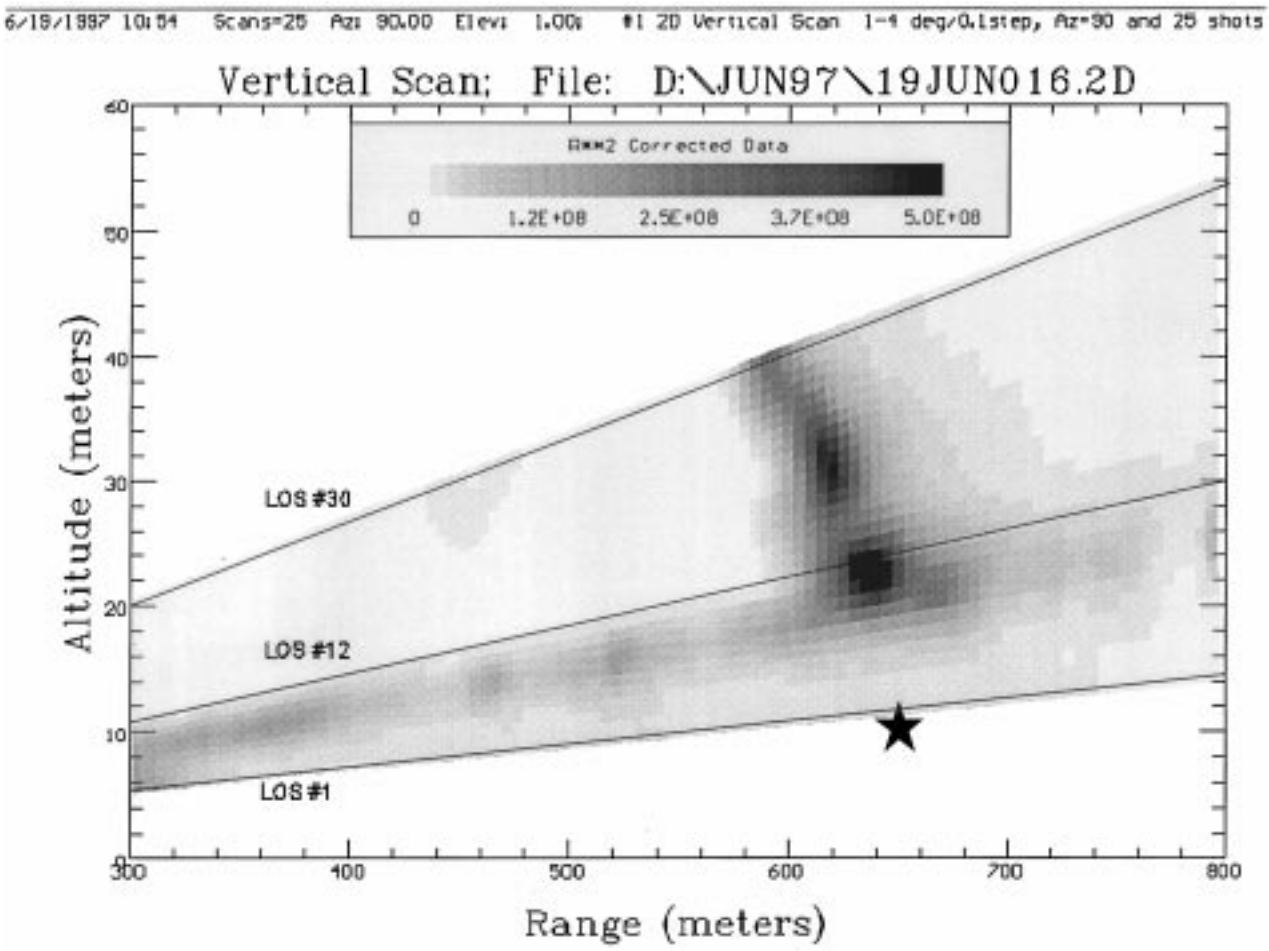


**FIGURE 3. Lidar 2D vertical scan collected along a plane downwind of the tractor (see Figures 1 and 2) by scanning the lidar 1−4 deg in elevation. The dust plume at ~650 m range extends up to 30 m height. Three of the 30 lines-of-sight that make up the scan image are indicated by the lines. The star shows the sampling location of a 10-m point sampler positioned 650 m from the lidar. Note that this sampler is well below the height of the dust plume.**

line-of-sight was immediately upwind of the point samplers located along the downwind edge of the field (Figure 2a). This position allowed two-dimensional vertical scans of the PM leaving the field during the harvesting or disk harrowing operations. The disking tractor operated at an angle of ~30° to the crosswind direction and traveled in an elongated concentric pattern (Figure 2b). Thus, the lidar scan plane was located at different distances downwind of the disking tractor source depending on tractor range (= radial distance along lidar LOS).

## Results and Discussion

**2D and TD Lidar Scans.** The lidar is capable of three types of scans: both two- (2D) and three-dimensional (3D) spatial scans and a temporal scan called a time−domain (TD) scan. Both the 2D and TD scans are discussed below to indicate the type of spatial and temporal resolution achievable with the lidar. The data contained within each of the different types of lidar graphical displays can be analyzed to estimate $PM_{10}$ emission factors for agricultural operations once suitable backscatter-PM mass calibration relationships are determined. Data analysis methods are currently under development and include the following: methods for integrating the lidar signal for calibration to $PM_{10}$ mass using point sampler data; spatial data analysis techniques for estimating plume dispersion properties; reconciling differences in the plume volume sampled by point sampler arrays and the entire plume dimensions outlined with the lidar; and time−series analysis of TD data for predictive modeling of PM emission factors and emissions variability. The results from some of these analyses are presented below after a brief description of the types of data collected with the lidar

**(a) 2D Scans.** By scanning the lidar either horizontally or vertically across the atmosphere, a 2D image of relative PM concentrations is developed from the individual lidar lines-of-sight. For example, 2D vertical scans show the distribution of particulate matter in a vertical slice through the atmosphere. A 2D vertical scan (Figure 3) taken with the lidar positioned downwind of a disking tractor (i.e., geometry in Figure 2) shows the dust plume at a range of ~650 m from the lidar and at a height between 15 and 30 m. The signal was collected with a range resolution of 5 m, a vertical resolution of 0.1 deg, and 25 summed laser pulses per LOS. The gray-shaded areas represent differences in the background-corrected lidar signal multiplied by $R^2$, as indicated by the legend scale bar. The entire scan was collected in less than 1 min but can be collected even faster by reducing the number of laser pulses per line-of-sight. Note the individual lines-of-sight as represented by the diagonal lines at increasing angles to the *x*-axis for the first, 12th, and last lines-of-sight. Vertical scans can be taken repeatedly along the downwind edge of a field in order to quantify the quantity and distribution of PM leaving the nonpoint source area. A conventional point sampler would cover only a small area on this vertical scan image. For example, a 10-m tower sampler at a range of 650 m is indicated by the star in Figure 3. Note that for this case, a significant portion of the PM flux from the field would have been missed by the point samplers

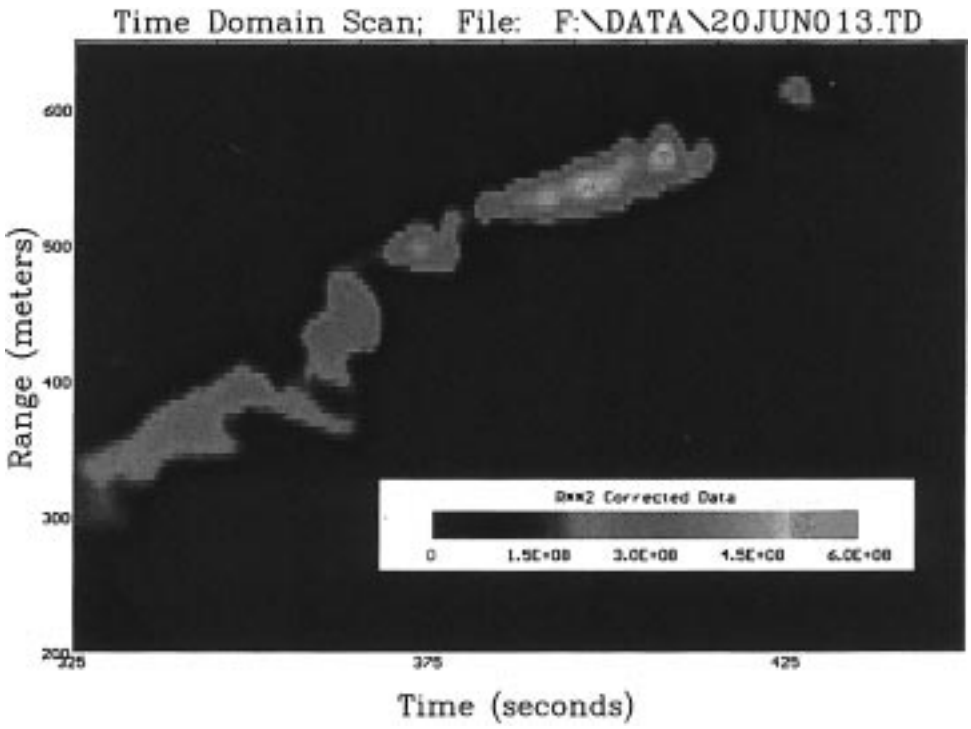


**FIGURE 4. Time−domain (TD) scan during first disking after wheat harvest. The tractor was upwind of the lidar as in Figure 2b, and the laser was held steady at an elevation angle of 2 deg during the scan. The signal represents the portion of the dust plume transported across the lidar's line-of-sight as a function of time. Since the range of the detected plume increases with time, the data indicate that the tractor was moving away from the lidar's side of the field. The slope of the dust plume signal is proportional to the tractor's speed, assuming steady wind conditions. Variations in the plume character (width, intensity) with time can be due to wind perturbations (speed or direction) or changes in the quantity of dust generated as the tractor crosses the field.**

because the dust plume was located at elevations above the highest PM sampler location.

**(b) TD Scans.** In a time−domain (TD) scan, range from the lidar is on the *y*-axis and time is on the *x*-axis. The lidar scanner does not move during a TD scan. Instead, the TD scans represent data collected from a specified number of laser pulses along a single line-of-sight for a scan duration (time) set by the user. A TD scan from a first disking agricultural operation (Figure 4) shows the dust plume generated by a tractor located upwind of the lidar. The plume appears as a diagonal line on the TD scan, representing increasing range of the dust cloud with time, because the tractor was moving away from the lidar's side of the field over the time period shown in the figure. Note that detailed temporal variations in the dust plume characteristics can be monitored with the TD scans. As discussed in more detail below, the TD scans obtained with the lidar (i.e., Figure 4) indicate that agricultural tractor operations such as disking can be reasonably modeled as moving point, or line, sources.

Time−domain scans can also be used to quantify the velocity of the aerosols, or the wind velocity, since the slope of the TD scan trace corresponds to velocity. By rapidly scanning the lidar between multiple LOS at an angle to the wind and determining relative aerosol displacements between the different lines, wind velocity can be monitored in real-time across a field. In contrast to previous efforts for determining wind speed using elastic lidar (*19*−*23*), where winds were obtained over scales of 1−5 km, accurate wind speed profile monitoring with the UCD miniature elastic lidar will achieve scales of 50−100 m, due to the higher spatial resolution of this instrument. This information is infinitely more useful than a single meteorological station or lower resolution lidar wind data for understanding pollutant plume transport and variability and is a capability of the lidar that does not require instrument calibration. The wind data can greatly improve nonpoint source $PM_{10}$ emission flux estimates made using point arrays by providing spatially averaged wind profile information and can aid in understanding the effects surface features (crops, barriers) have on boundary layer flow.

**Lidar Data Analysis. (a) Vertical and Horizontal Extent of Dust Plumes.** The 2D vertical scans made at the downwind edge of the field during first disking (Figure 5) indicate that the dust plumes generated by the tractor operations repeatedly reached heights of 20−40 m. This is clearly shown in the two scans taken 20 min apart (Figure 5) when the tractor was located in about the same crosswind location (see Figure 2b). Each of the scans was collected in 32 s. Clearly, the 2D data records the fugitive dust plume dimensions and structure in tremendous detail across the entire downwind plane of the nonpoint source (the field).

Data analysis methods are under development to use repeated 2D vertical scans collected along a single plane at the field downwind boundary to determine relative PM fluxes. Cross-sections of the plume over time can be calculated by integrating the 2D scan data over appropriate time intervals. An appropriate time interval would be the amount of time it takes for the tractor to traverse the field since the dust source could then be modeled as a finite line source. Data collection parameters that must be optimized for this analysis include lidar scan rate relative to both source and wind speeds and lidar azimuth relative to wind direction. Once validated, these techniques will give unparalleled information of PM flux variability both in space and time.

In an analogous manner, horizontal plume characteristics can be obtained using 2D horizontal scans. Furthermore, 3D scans can be made, albeit over longer time intervals, by conducting a series of horizontal scans at different elevations in a given region of the atmosphere.

**(b) Effect of Distance from Operation on Plume Characteristics.** With the lidar scanning plane fixed and parallel to the downwind boundary of the field (i.e., Figure 2), the tractor's distance upwind from the lidar 2D measurement

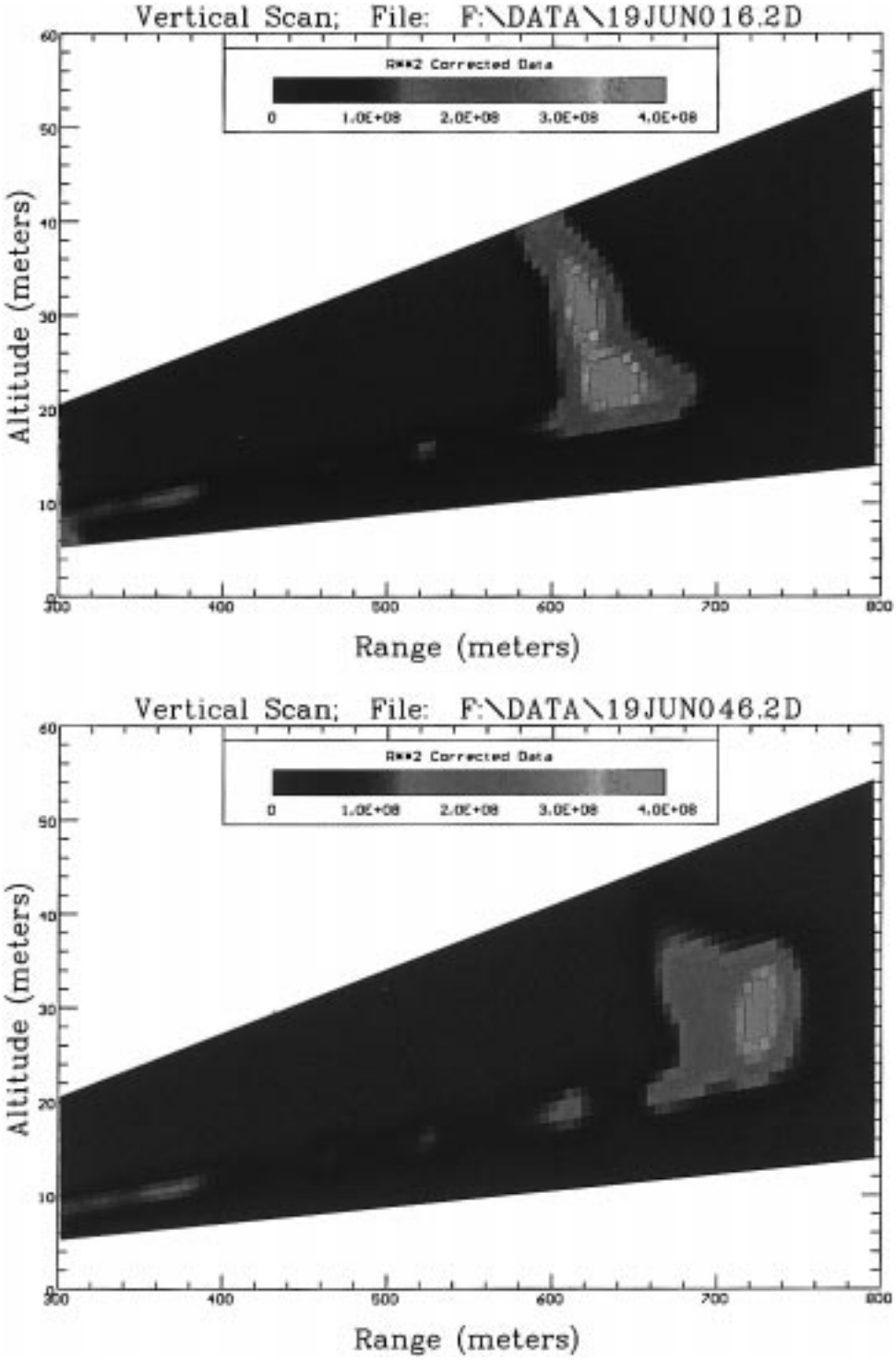


**FIGURE 5. Vertical 2D scans collected at times 20 min apart. The approximate positions of the tractor on the field during these two scans are indicated in Figure 2b. The first scan (panel a, top) was collected at 10:54 a.m. and panel b (bottom) was collected at 11:14 a.m. when the tractor was located farther upwind from the lidar scan plane. Note the increased plume size in panel b.**

plane generally increased with time as the tractor worked its way up the field. For stable wind speed and direction conditions, dispersion theory predicts that the physical dimensions of the plume cross-section sampled by the lidar 2D scan should increase as the distance of the sampling plane from the source increases. The data in Figure 5 support this expectation. The first scan (Figure 5a) was collected at 10:54 a.m. when the tractor was approximately 20 m closer to the lidar scan plane than the second scan (Figure 5b) collected at 11:14 a.m. Clearly, the plume was larger in the latter scan (Figure 5b) when the tractor source was farther upwind, as expected. Wind speed and direction at four sampling heights during the 20-min time interval represented by the data in Figure 5 was relatively steady (Figure 6).

Time−domain scans (Figure 7) also indicate that the plume dimensions changed as the tractor traveled across the field, but for different reasons. In Figure 7, for a given range there is appreciable variability in the plume width (measured in range) as a function of time. These changes can be caused by variations in tractor speed, soil moisture, surface roughness, and wind speed and direction. Transects of the TD data in Figure 7 at three different times when the

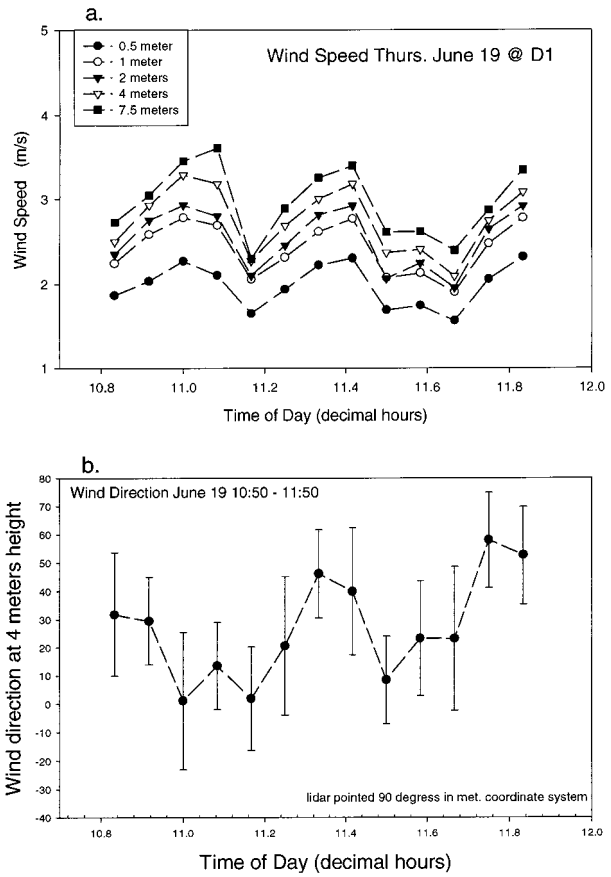


**FIGURE 6. (a) Wind speed data for five heights at the downwind meteorological tower and (b) wind direction at 4 m for the sampling period represented by the data in Figure 5. The wind speed increased with height as expected and was relatively constant over the PM sampling period. Wind direction is based on 5-min averages of data collected every 10 s. Error bars are one standard deviation.**

tractor was crossing the same range location indicate how the crosswind dimensions of the plume in a TD scan depend more strongly on wind conditions than on tractor upwind distance from the lidar scan plane (Figure 8). This is especially true for TD scans under variable wind conditions because the single beam line of the TD scan may intercept different vertical sections of a dispersing plume at different times. Since a 2D scan captures the entire plume cross-section, both vertically and horizontally, it is not subject to this limitation. Thus, 2D vertical scans collected at multiple downwind planes are better suited than TD scans for quantifying and modeling plume long-range transport parameters (i.e., dispersion coefficients).

The plume character during the turns at the far field boundary was often highly variable compared to the mid-field plume traces (see Figure 7). Partly this was due to the fact that the TD scan stationary lidar beam was at a 2 deg elevation angle that allowed portions of the dust plume to pass below the lidar LOS at far ranges (where the beam was at higher elevations). For example, in Figure 7, the beam height was 28 m at a range of 800 m. Therefore, while TD scans are useful for monitoring a particular location or line-of-sight over time and serve to confirm that tractor operations are $PM_{10}$ line sources (i.e., integrated moving point source $\simeq$ line source), in general, 2D scans are better tools for capturing the entire plume. Furthermore, these observations suggest that fast-scanning lidar instruments will be necessary to measure PM emission factors most reliably.

**(c) TD Scans Indicate Line Sources during Tractor Operations.** The dust plume locations with time in the TD scans track the movement of the tractor across the field and allow real-time monitoring of the number of times the implement passed directly upwind of the fixed point sampler array. The zigzag pattern (Figure 7) is due to the tractor turning around at the far crosswind field boundary located at a range of ~800 m (dirt road). When the tractor moved toward the lidar's side of the field, the lidar recorded a plume trace with a negative slope in Figure 7 since the plume (which strongly follows the tractor crosswind position in all the lidar data) range decreased with time. The repeated pattern of these scans as the tractor crossed the field indicates that if each pass is considered a unit of operation for the calculation of emission factors, then a finite line source is a very good mathematical approximation of these agricultural activities. Combined with meteorological data collected with sufficient temporal and vertical resolution, the lidar data can be used to develop and validate a fugitive dust dispersion model for nonpoint agricultural $PM_{10}$ sources.

**(d) Estimate of Total Dust Fraction Sampled by Point Samplers.** It is clear from the discussion of Figures 3 and 5 that the point sampling array was undersampling the fugitive dust plume emitted during the disk harrowing operation. The plume was detected at heights well above the 9 m height of the highest point sampler. This was true even considering the fact that the sampling tower was located within 10 m downwind of the operation at the start of the sampling test. This observation has two implications: (i) $PM_{10}$ emission factors calculated from the point sampler data collected during this test will be biased low and (ii) the use of portable PM sampling towers that can be moved close to the tractor line source and maintain a fixed distance to the line source for the duration of the test will provide the most reliable estimates of $PM_{10}$ emission factors.

However, it should be kept in mind that following the tractor down the field can result in overestimates of the amount of $PM_{10}$ that will actually leave the field due to the difficulty of estimating the amount of dust that will dry deposit within the field boundaries. In addition, roving PM samplers still require long integration times for $PM_{10}$ mass quantification relative to the temporal resolution possible with lidar. Therefore, we propose that simultaneous use of lidar downwind of the source (at multiple downwind scan planes) and roving point $PM_{10}$ samplers closer to the source will provide the best data for both quantifying and chemically characterizing agricultural $PM_{10}$ emissions.

A data analysis technique to estimate the fraction of the plume that is actually sampled by the point samplers from the lidar 2D scan data is under development. The technique is based on determining the relative geometric areas of the PM sampler 'volume' and the total plume in a 2D scan and calculating the ratio of the integrated lidar signal over these areas. These calculations will provide estimates of the amount of fugitive dust that is 'missed' by fixed point samplers. This information is critical to improving $PM_{10}$ emissions estimates and can be obtained without lidar calibration.

**(e) Modeling Agricultural $PM_{10}$ Emissions.** The lidar data can be used directly to estimate horizontal and vertical dispersion coefficients for the agricultural dust plumes. These estimates can be compared with estimates based on other techniques such as thermal stability and wind gradients. It will be important to use the lidar to assess how the plume characteristics vary with type of agricultural operation as well as environmental factors such as soil moisture, temperature, and bed and irrigation techniques. This information combined with data on variations in $PM_{10}$ emissions by implement type, soil, and meteorological properties will enable development of a line-source model for agricultural field operations. Such a model will allow predictions of air quality to be made based on a wide range of forcing

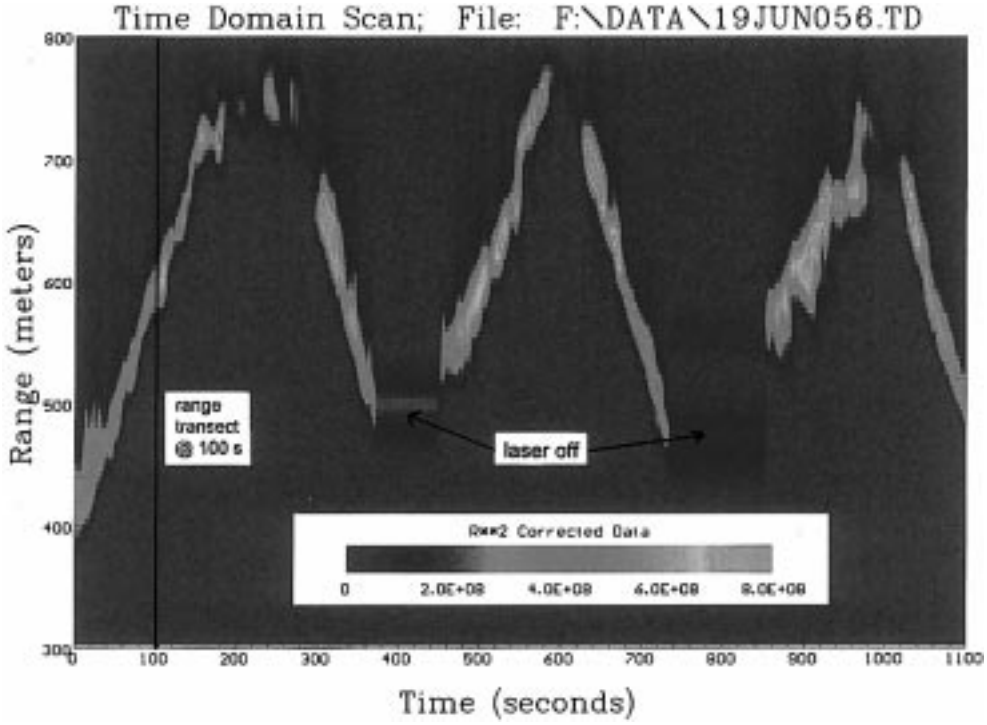


**FIGURE 7. TD scan from first disking operation. Data were collected after the 2D scans (e.g., Figure 5). The sawtooth pattern of the dust plume signal clearly indicates the line source nature of these types of tractor operations. The lidar was positioned as in Figure 2. The tractor turned around at the far side of the field at ~800 m range. When the tractor was located on the lidar side of the field, the laser was turned off during times when the tractor was in the lidar line-of-sight (i.e., 400 s). The range transects in Figure 8 represent data collected along lines such as that indicated for the 100-s scan.**

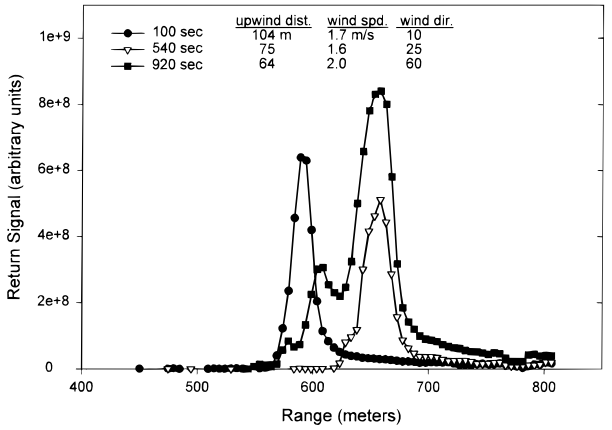


**FIGURE 8. 1D range transects extracted from the TD data in Figure 7 (see transect line at 100 s). The approximate upwind distance to the tractor and wind speed and direction during each transect time are indicated. Note that crosswind plume dimension does not correlate well with upwind distance for TD scans.**

mechanisms and environmental conditions and will enable development of reasonable mitigation strategies for different types of crops or different operations.

Finally, the lidar can be used to measure wind velocity and direction, as mentioned previously. This application requires implementing 2D cross-correlation algorithms for TD scans, but the payoff for this effort will be substantial in terms of improved temporal and spatial resolution for field-wide flux calculations.

**(f) Lidar and Point Sampler Capabilities.** Lidar has three unique advantages over conventional point samplers: (i) higher spatial resolution, (ii) higher temporal resolution, and (iii) greater spatial range, both vertically and horizontally. These factors make lidar an ideal choice for quantifying the dimensions and dynamics of aerosol plumes under field conditions. For example, the maximum vertical height that can be sampled with conventional PM samplers is limited to the height of an erected tower or a building near the measurement site. Most portable field towers are about 10 m in height, and buildings are not ideal sampler locations due to the effect they have on local wind patterns.

Point sampling arrays have the advantage of providing dust samples for laboratory chemical analysis but suffer from spatial and temporal resolution limitations. Unfortunately, the use of point PM filter samplers requires collection of integrated samples over times of up to 2 h in order to quantify PM mass via gravimetric analysis. During this time period, the spatial relationship between the samplers and the PM source (the agricultural implement) changes dramatically as the implement traverses the field. Thus, the poor temporal resolution of point samplers hinders data interpretation and the development of predictive emission models. Spatial resolution is also limited to a handful of point locations downwind of the source with little crosswind information. Obtaining the crosswind data could be especially important if implement turning operations at the edges of the field generate a significant amount of PM.

By contrast, the lidar can easily scan thousands of meters horizontally and vertically to determine relative aerosol concentrations. For example, a 20 deg elevation LOS samples at a height of 180 m at a range of 500 m from the lidar. Thus, the vertical spatial scales that can be probed easily by the lidar represent a significant improvement over point samplers. Add to this the fact that the lidar is capable of range resolution on the order of 3 m, and the lidar further improves the ability to quantify particulate matter emission factors and plume geometry. The only limitation on vertical range is the presence of thick scattering regions (such as fog or very dense plumes) because the laser beam cannot penetrate these bodies.

Another advantage of lidar over point sampling methods is that both the upwind and downwind locations can easily

and quickly be changed with time. This means that individual upwind background scans can be coupled to downwind sample scans even under varying wind conditions.

In addition to its capability for delimiting the spatial distributions of an aerosol plume at a given time, the lidar's fast-scanning capabilities give it tremendous temporal resolution and allow one to monitor plume dynamics over time. A typical 2D vertical scan (over 20 deg at 0.2 deg steps and 25 laser pulses) is acquired in less than 1 min. This scanning time can be decreased if one reduces the number of laser pulses or increases the step angle. Together with high time−resolution meteorological data, the lidar enables essentially real-time, detailed studies of the dynamics of aerosol plumes. The high-resolution capabilities of the lidar currently provide unparalleled information on the natural variability of agricultural fugitive dust plumes. This information is critical to accurately estimating realistic agricultural operation emission factors for use in $PM_{10}$ regional air quality plans.

**(g) Lidar Calibration for $PM_{10}$ Emission Rates.** $PM_{10}$ emission rates, *E*, can be quantified using spatially integrated lidar vertical scans downwind of the nonpoint source (*24*−*26*):

$$E = \int u \sin\theta \, P(R) \, dA \qquad (3)$$

where *u* is the wind velocity, $\theta$ is the angle between the lidar plane and the wind direction, and *P*(*R*)is the lidar signal, all integrated over the cross-sectional area of the plume. The conversion of the integrated lidar signal to $PM_{10}$ concentration depends on determining the calibration relationship between backscatter, extinction, and $PM_{10}$ particle mass concentration.

Because the lidar signal depends on the optical scattering properties of the PM and these optical properties vary with particle shape, composition, and particle size distribution as well as PM concentration, the lidar signal must be calibrated to $PM_{10}$ mass in order to obtain emission factors directly. Calibration procedures used in the past (*27*−*30*) have used hard targets of known reflectivity at close range; but using targets requires attenuation in order to protect the lidar detector. We are developing a new calibration procedure that allows calibration under actual instrument field conditions. These calibration tests will involve (i) simultaneous collection of lidar TD scans immediately upwind of point filter samplers over the entire duration of a filter ($PM_{10}$ mass concentration) measurement test, (ii) the use of a new reflective target profiling method during field operations for in situ calibration, and (iii) calibration tunnel experiments using a wide range of agricultural soils as dust sources. The calibrations will provide information on how dust composition, size distribution, and particle mass, and number density ($PM_{10}$ concentration) affect the lidar return signal. Once calibration is complete, the lidar will be used to directly quantify $PM_{10}$ emission factors from a wide range of agricultural operations.

Current lidar capabilities that do not depend on complete calibration of the lidar to $PM_{10}$ mass include (i) identifying locations for siting fixed point samplers to improve fugitive dust plume capture; (ii) providing quantitative information on plume undersampling by point arrays; (iii) higher resolution wind measurements on 50−100 m scales; (iv) providing information on plume variability within and between different types of agricultural operations; and (v) determining plume dispersion coefficients for modeling plume transport.

The best future sampling programs for fugitive dust will employ lidar to obtain improved spatial and temporal resolution in $PM_{10}$ flux estimates in addition to using strategically placed point samplers, both for lidar ground-truthing and to obtain dust samples for chemical analysis. Combined with high temporal resolution meteorological data, derived either from lidar wind analysis routines or conventional tower arrays, development of a robust model for predicting agricultural $PM_{10}$ emissions under different environmental conditions will be practical.

## Acknowledgments

Support was from USDA Special Research Grants Program via Grant 94-33825-0383 and 98-38825-6063.

## Literature Cited

(1) Glotfelty, D. E.; Leech, M. M.; Jersey, J.; Taylor, A. W. *J. Agric. Food Chem*. **1989**, *37*, 546.
(2) Glotfelty, D. E.; Schomburg, C. J.; McChesney, M. M.; Sagebiel, J. C.; Seiber, J. N. *Chemosphere* **1990**, *21*, 1303.
(3) Seiber, J. N.; Woodrow, J. E. *Eighth International Congress of Pesticide Chemistry: Options 2000*, Washington, DC 1995; American Chemical Society: Washington, DC, 1995; p 157.
(4) Matsumura, R. T.; Flocchini, R. G.; Cahill, T. A.; Carvacho, O.; Lu, Z. *$PM_{10}$ Standards and Nontraditonal Particulate Source Controls*; Air & Waste Management Association: Pittsburgh, 1992; p 417.
(5) Cowherd, C., Jr. In *Aerosol Measurement: Principles, Techniques, and Applications*; Willeke, K., Baron, P. A., Eds.; Van Nostrand Reinhold: New York, 1993; pp 640−658.
(6) Ashbaugh, L.; Matsumura, R.; James, T.; Carvacho, O.; Flocchini, R. International Conference on Air Pollution from Agricultural Operations, Kansas City, MO, Feb 7−9, 1996.
(7) Clausnitzer, H.; Singer, M. J. *J. Environ. Qual.* **1996**, *25*, 877.
(8) Clausnitzer, H.; Singer, M. J. *Calif. Agric.* **1997**, *51*, 27.
(9) Collis, R. T. H.; Russell, P. B. In *Laser Monitoring of the Atmosphere*; Hinkley, E. D., Ed.; Springer-Verlag: New York, 1976; Vol. 14, p 71.
(10) Measures, R. M. *Laser Remote Sensing*; Wiley-Interscience: New York, 1984.
(11) Klett, J. D. *Appl. Opt.* **1981**, *20*, 211.
(12) Klett, J. D. *Appl. Opt.* **1985**, *24*, 1609.
(13) Elterman, L. *Atmospheric Attenuation Model in the Ultraviolet, Visible, and Infrared Regions for Altitudes to 50 km*; AFCRL-68-0153; A. F. Cambridge Research Laboratories: Hanscom Field, MA, 1964.
(14) van de Hulst, H. C. *Light Scattering by Small Particles*; Dover Publications: New York, 1981.
(15) McCartney, E. J. *Optics of the Atmosphere*; John Wiley & Sons: New York, 1976.
(16) Hofeldt, D. L.; Olson, B. A. *Optical Remote Sensing of the Atmosphere*; Optical Society of America, Santa Fe, NM, 1997; p 65.
(17) Flanigan, D. F.; Delong, H. P. *Appl. Opt.* **1971**, *10*, 51.
(18) Walter, D. P.; Cooper, D. E.; van der Laan, J. E.; Murray, E. R. *Appl. Opt.* **1986**, *25*, 2506.
(19) Eloranta, E. W.; King, J. M.; Weinman, J. A. *J. Appl. Meteorol.* **1975**, *14*, 1485.
(20) Sroga, J. T.; Eloranta, E. W. *J. Appl. Meteorol.* **1980**, *19*, 598.
(21) Schols, J. L.; Eloranta, E. W. *J. Geophys. Res.* **1992**, *97 (D17)*, 18395.
(22) Hooper, W. P.; Eloranta, E. W. *J. Climate Appl. Meteorol.* **1986**, *25*, 990.
(23) Kolev, I.; Parvanov, O.; Kaprielov, B. *Appl. Opt.* **1988**, *27*, 2524.
(24) Uthe, E. E.; Lapple, C. E.; Witham, C. L.; Mancuso, R. L. Third Symposium on Fugitive Emissions Measurement and Control, San Francisco, CA, 1979; EPA-600/7-79-182; U.S. EPA: Washington, DC, 1979; p 431.
(25) Uthe, E. E. *J. Air Pollut. Control Assoc.* **1980**, *30*, 382.
(26) Uthe, E. E. *Appl. Opt.* **1981**, *20*, 1503.
(27) Jarzembski, M. A.; Srivastava, V.; Chambers, D. M. *Appl. Opt.* **1996**, *35*, 2096.
(28) Hall, F. F. J.; Ageno, H. Y. *Appl. Opt.* **1970**, *9*, 1820.
(29) Jorgensen, H. E.; Mikkelsen, T.; Streicher, J.; Herrmann, H.; Werner, C.; Lyck, E. *Appl. Phys. B* **1997**, *64*, 355.
(30) Haner, D. A.; Menzies, R. T. *Appl. Opt.* **1993**, *32*, 6804.

*Received for review February 23, 1998. Revised manuscript received June 1, 1998. Accepted July 9, 1998.*

ES980176P